Applied Materials Today 14 (2019) 102–107

Contents lists available at ScienceDirect

Applied Materials Today

journal homepage: www.elsevier.com/locate/apmt

Local strain mapping of GO nanosheets under in situ TEM tensile testing

Changhong Cao[a,1], Zhuoran Zhang[a,1], Maedeh Amirmaleki[a], Jason Tam[b], Wenkun Dou[a], Tobin Filleter[a,*], Yu Sun[a,*]

[a] Department of Mechanical and Industrial Engineering, University of Toronto, 5 King's College Rd, Toronto, ON M5S 3G8, Canada
[b] Department of Materials Science and Engineering, University of Toronto, 184 College St, Toronto, ON M5S 3E4, Canada

ARTICLE INFO

Article history:
Received 16 July 2018
Received in revised form
13 November 2018
Accepted 21 November 2018

Keywords:
2D materials
Strain mapping
in situ TEM
Graphene Oxide
MEMS

ABSTRACT

Local strain mapping of 2D materials at nanoscale under continuous deformation can enable a variety of studies on 2D materials including but not limited to more accurate characterization of physical properties, heterogeneity characterization of functionalized 2D materials, and strain engineering of 2D materials. Here, using graphene oxide (GO) as a representative material, we report a technique that achieves local strain mapping of 2D materials at nanoscale through gold nanoparticle decoration over GO under in situ TEM tensile testing and imaging. Our results reveal that GO at different uniaxial tensile strain levels exhibits a heterogeneous local strain distribution. Using this technique, the permanent deformation of GO was also quantified to be ~1% on average. The technique can be readily applied to the strain mapping of other 2D materials.

1. Introduction

Strain mapping is important for characterizing material properties and for strain engineering [1]. Digital image correlation (DIC) is a key method for strain mapping and has been widely applied to quantify in-plane deformation [2]. The DIC method was used for strain mapping on macroscopic materials ranging from soil [3], to metals [4] and to rubbers [5], and is also applicable to measuring materials at nanoscale. Several strain mapping techniques implementing the DIC method have been applied to 2D materials including electron/x-ray diffraction which captures changes in diffraction patterns induced by strain [6,7] and Raman spectroscopy which monitors the characteristic vibrational energy levels of the material [8]. Both techniques were usually limited to mapping residual strain when a material is in a steady state [9–13]. Recently, Raman spectroscopy was coupled with other equipment to obtain strain mapping of 2D materials under quasi-static loading. For example, by applying deformation via atomic force microscopy [14] or bulging test apparatus [15], Raman spectroscopy was performed to measure the strain variation across graphene samples for mechanical characterization. Despite the capability for strain mapping of 2D materials, this technique requires a high number of Raman spectra and a complex experimental setup, which is challenging and time-consuming; and due to the large spot size of Raman laser (μm), the obtained strain maps are limited to the micro-scale.

Here, we report a technique for nanoscale strain mapping of 2D materials while the material is under continuous uniaxial tension. Graphene oxide (GO) was used as a representative 2D material in this study.

2. Results

GO-Au solution was prepared by mixing citrate-stabilized gold nanoparticles (AuNPs) with GO-water solution (see Section 4). In water, the electrical double layer of the GO nanosheets is able to attract and capture AuNPs in a controllable manner without the need for additional chemical linkers [16]. GO-Au solution was then drop cast onto a microelectromechanical systems (MEMS) tensile testing device [17] and air dried to form suspended GO-Au nanosheet over the actuation shuttles (Fig. 1). The transmission electron microscopy (TEM)-compatible MEMS device enables in situ characterization [18]. The MEMS device with suspended GO-Au nanosheet was examined under scanning transmission electron microscopy mode (STEM) with simultaneous secondary electron (SE) and high angle annular dark field (HAADF) imaging to check the quality as well as the distribution of AuNPs. As Fig. 1a and b shows, the nanosheet before tensile test had no observable cracks or damage, and AuNPs attached to the nanosheet were uniformly

* Corresponding authors.
E-mail addresses: filleter@mie.utoronto.ca (T. Filleter), sun@mie.utoronto.ca (Y. Sun).
[1] These authors contributed equally to the work.

https://doi.org/10.1016/j.apmt.2018.11.010
2352-9407/

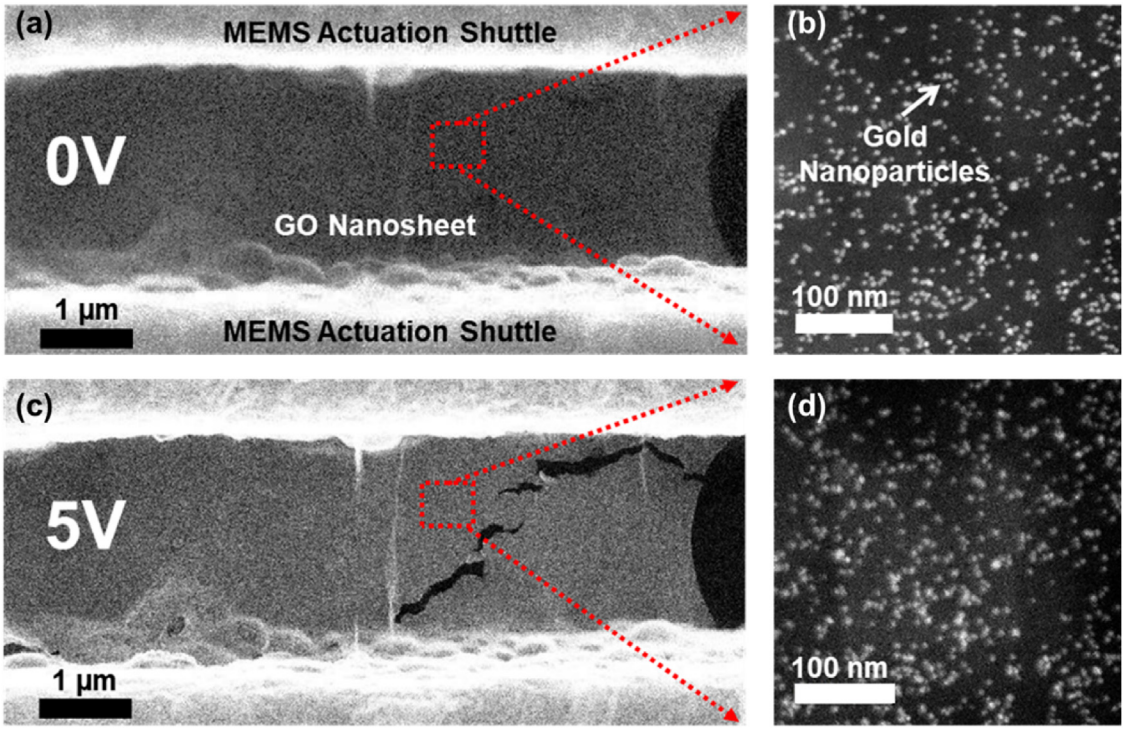

Fig. 1. SE (a, c) and HAADF (b, d) images of in situ STEM tensile testing of gold nanoparticle-decorated GO nanosheet on a MEMS tensile testing device. (a) Gold nanoparticle-decorated GO nanosheet suspended over MEMS actuation shuttles when no voltage was applied to the MEMS device; (b) region dash-boxed in (a) at high magnification; (c) GO nanosheet in (a) when 5 V was applied to the MEMS device; failure of the nanosheet occurred; (d) region dash-boxed in (c) at high magnification. (b) and (d) are the same region on the nanosheet.

distributed. Subsequently, voltage in increasing steps was applied to the MEMS device to perform tensile test of the GO-Au nanosheet in situ STEM. SE images of the entire nanosheet as well as HAADF images of a selected area at high magnification were captured at different actuation voltages (Fig. 1). Actuation voltages were applied up to 5 V when the nanosheet failed (with an increment of 0.5 V) and apparent cracks were observed on the nanosheet (Fig. 1c). Movement of AuNPs were captured by HAADF imaging (Fig. 1b and d) and analyzed by image processing to generate local strain maps in the loading direction.

Extracting the positions of AuNPs was the first step toward local strain mapping. As shown in Fig. 2a, the original image was first median filtered to reduce background noise. The noise-filtered image was binarized using Otsu's thresholding method [19]. The Otsu's method was used because it maximizes the inter-class variance between background and foreground objects [19]. Morphological opening operation was followed to further remove noise in the binarized image. Contour of the particle was then extracted from the binarized image and the centroid of each contour of the AuNP was calculated for each particle. Among many contours, AuNPs were manually identified across images at different voltages via computer mouse clicking. This minimal manual input eliminates potential errors caused by mismatching the AuNPs.

Since imaging noise can cause an AuNP to appear different in shape in different TEM images and cause errors in calculating centroids of AuNPs, this error was further reduced by template matching (Fig. 2a). The binary image incorporating each AuNP before tensile testing (i.e., in the 0 V image) was saved as the template image and compared with the images at other actuation voltages. Poorly matched AuNPs were rejected from the strain map. This method was also effective in rejecting AuNP clusters, whose shape may change under different actuation voltages, from strain calculation. The measurement process was repeated for all AuNPs and on images captured at different actuation voltages.

When local strain mapping was generated, "local" was defined as a circle centering at an AuNP's centroid with radius r. All neighboring AuNPs located within the circle were used for strain calculation (Fig. 2b). In order to incorporate a reasonable number of AuNPs, we set the radius r to be adaptive to the distance between neighboring AuNPs:

$$r = K \times \max(d_{ij}), \tag{1}$$

where d_{ij} is the distance between the arbitrary neighboring ith and jth AuNP, and K is a coefficient adjusting the radius and the number of AuNPs included for strain calculation. $K = 6$ was chosen in this work to reflect strain within a radius of approximately 100 nm to each AuNP such that it is not too small that only few AuNPs were available for strain mapping, nor too large that the calculated strain was influenced by the global strain.

It should be noted that all strain values in this work were only measured in the loading direction (longitudinal) as strain perpendicular to the loading direction was negligible. For strain mapping within each local region r, the longitudinal strain between two neighboring AuNPs was defined as the strain at the midpoint between the particles.

$$strain\left(\frac{x_0^c + x_k^c}{2}, \frac{y_i^c + y_j^c}{2}\right) = \frac{(y_0^c - y_k^c) - (y_0^{0V} - y_k^{0V})}{(y_0^{0V} - y_k^{0V})}, \tag{2}$$

where $\left(x_0^c, y_0^c\right)$ and $\left(x_k^c, y_k^c\right)$ denote centroids of the central AuNP and an arbitrary kth AuNP in r, respectively; and $\left(x_0^{0V}, y_0^{0V}\right)$ and $\left(x_k^{0V}, y_k^{0V}\right)$ denote the centroids of the same AuNPs but in the 0 V image. Strain calculations were first looped for every AuNP within r, then switched the central AuNP to a different AuNP and repeated the previous step until every AuNP was used as the central point.

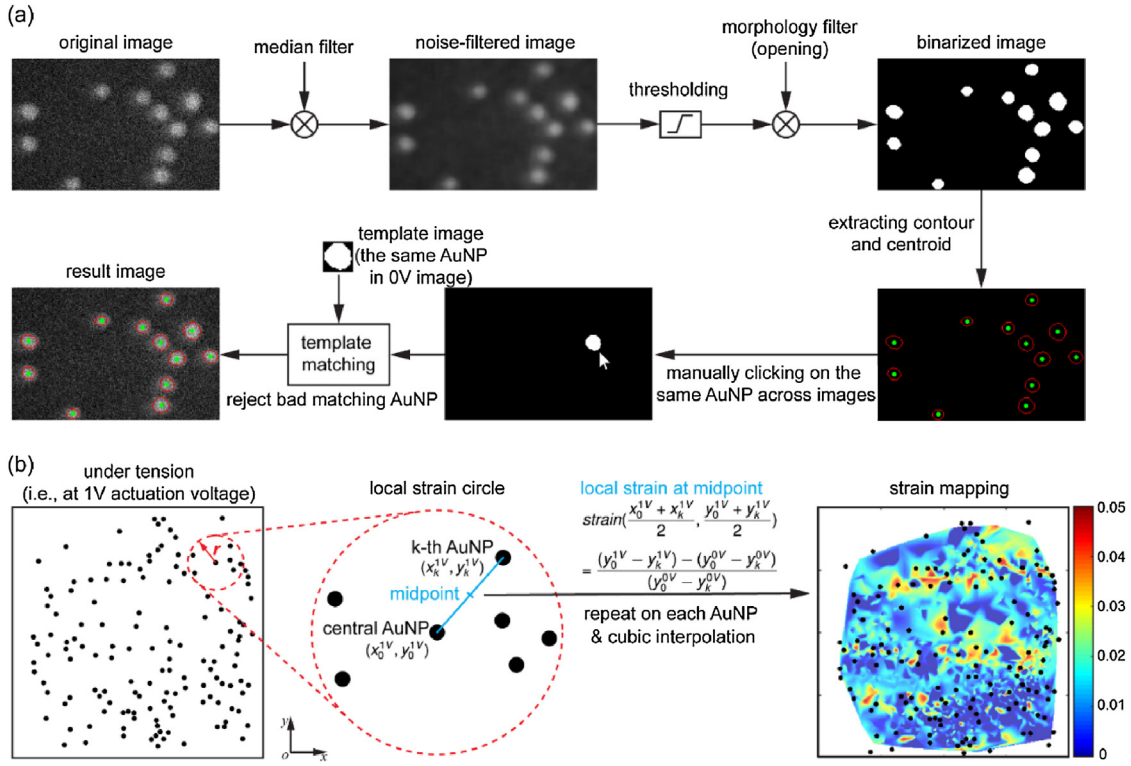

Fig. 2. Flowchart illustrating the image processing procedure for strain mapping. (a) The sequence of image processing for extracting AuNP positions. The original image (only sub-region shown) was filtered and binarized to extract the contour and centroid of each AuNP. The same AuNP across images at different actuation voltages was manually identified via computer mouse clicking. To eliminate the error caused by changes in the shapes of AuNPs, template matching with the image at 0 V was performed to each AuNP. Mismatched AuNPs were discarded for strain calculation. (b) Strain was calculated by comparing the distance between every pair of AuNPs within a local circle defined around a central AuNP at different actuation voltages. The calculated strain of each pair was used as the strain value for the midpoint of the two AuNPs. After calculating strain for every pair of AuNPs in a local circle, calculation continued with the next AuNP as the central point and repeat the previous step until every qualified AuNP was used as the central point. Bicubic interpolation was applied to obtain continuous strain mapping. The custom-written image processing code is publicized at: https://github.com/zhuoran0/GO-Strain-Mapping.

A total number of ~2000 discrete strain values was obtained in a selected 358 nm by 358 nm region (Fig. 1b and d). Finally, bicubic interpolation was applied to obtain continuous strain mapping (Figs. 2b and 3).

The generated strain maps of the selected area (Fig. 1b and d), with AuNPs overlaid at their true locations, are shown in Fig. 3. At 0 V, strain was assumed to be zero in the entire selected area and used as the benchmark for strain calculations at higher actuation voltages. As the actuation voltage increases, local strain increased, and an uneven local strain distribution was observed, which can be attributed to the complex stress state locally due to several potential factors including but not limited to: (i) oxygen functional groups on the GO basal plane are randomly distributed [20] and carbon atoms with functional groups attached are easier to be strained compared with those without functionalization; (ii) the randomly distributed functional groups can also result in complex interlayer interactions among GO layers [21–23]; (iii) structural defects in GO nanosheet, such as vacancies, dislocations, and grain boundaries which can cause local stochastic strain distribution [24,25]. At 5 V when the GO-Au nanosheet failed (Fig. 1c), an overall decrease of local strain can be observed, and residual strain was present after the nanosheet failed (Fig. 3). When the load was completely released, residual strain still retained, and the strain map shows no noticeable difference compared with the map at 5 V. This directly reflects the plastic deformation of GO when the GO nanosheet was stretched to failure. It has been reported that due to the oxygen functional groups, GO exhibits permanent deformation [23,26] while grapheme [27] does not. Nevertheless, permanent deformation was only indirectly inferred via force curves and fracture images at microscale [23,26] or via theoretical calculations [28] while our result provides direct evidence of permanent deformation at the nanoscale.

Discrete strain values at selected actuation voltages before interpolation were also plotted into a histogram (Fig. 4a) to further display the overall local strain variation. It is consistent with strain maps shown in Fig. 3 that a higher voltage causes local strain to shift toward higher values in general and an apparent local residual strain can be observed after load release.

Strain was also calculated globally by measuring the change in gap distance between the two actuation shuttles at different voltages, using the measurement method we previously reported [28]. As Fig. 4b shows, the average local strains in the selected area (Fig. 1b and d) calculated using data in Fig. 4a are within the error margin of global strains at each voltage. Global strain measurement has intrinsic large errors due to limited measurement resolution resulting from the low breaking-strain to nanosheet size ratio. This is not unique to GO, but 2D materials in general are brittle and fail at low strains [29,30]. The global strain at 5 V was deemed as zero because the nanosheet failed and global strain cannot be properly defined. In contrast, local strain mapping not only provides a detailed strain distribution in a fine area but also enables quantitative strain analysis, for instance, the average residual strain was calculated to be ~1% in the selected area of the sample shown in Fig. 1.

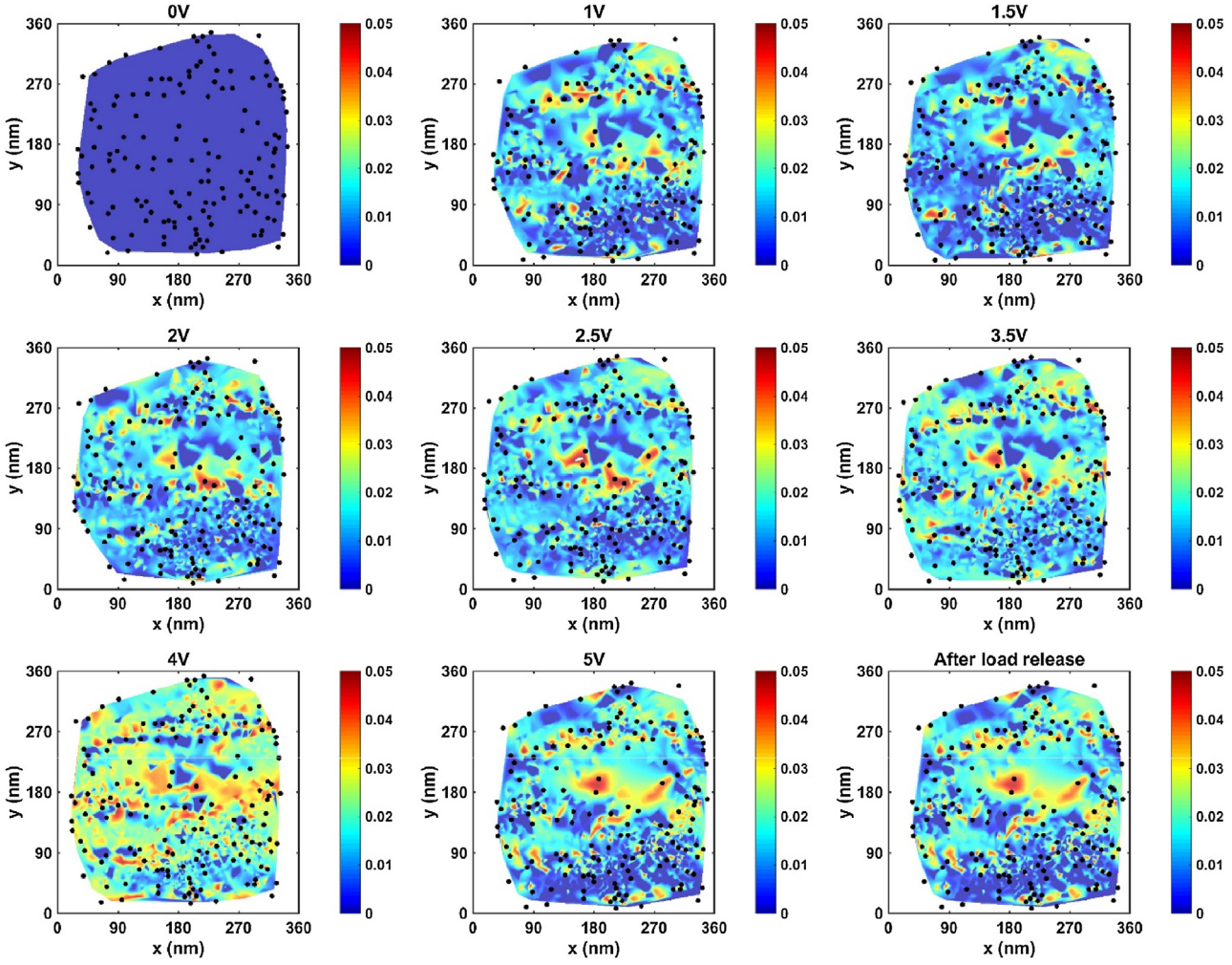

Fig. 3. Strain mapping of the selected area in Fig. 1b and d at different actuation voltages; black dots represent the relative positions of AuNP decorations on GO nanosheet, overlaid on top of the strain maps. Strain can be mapped locally at the nanometer scale and higher local strain can be observed with increasing actuation voltages in general; when the nanosheet failed at 5 V and after the load was released, residual strain was retained in the nanosheet.

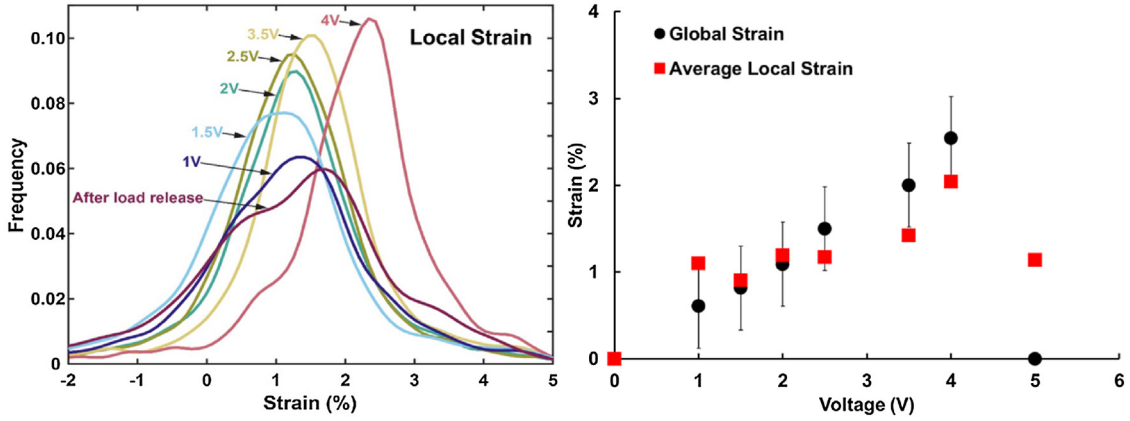

Fig. 4. (a) Contour of histogram showing the distribution and frequency of local strain at different actuation voltages in Fig. 3; local strains statistically increase at increased voltages; when load was released, residual stain can also be observed statistically; (b) both average local and global strain were plotted as a function of actuation voltage; average local strains were measured to be within the error margins of global strains at all voltages except at 5 V due to the uncertainty of global strain measurement when the nanosheet failed. Error bars of average local strain are small and buried in marks.

3. Conclusions

In summary, a technique that enables local strain mapping of 2D materials during tensile test was demonstrated. Heterogenous local strain distribution was observed on GO, and the average local strain increased with higher global strain in general. Permanent deformation of GO was observed and quantified using the quantitative technique. This technique can be readily applied for local

strain mapping of other 2D materials and can be integrated with other technologies to provide more comprehensive information. For example, electron diffraction pattern has the limitation of tracking strain only when the material is at a steady state. This limitation can be conquered by integrating electron diffraction with the current technique, which can enable strain mapping of 2D materials through the thickness while under quasi-static loading.

4. Experimental

4.1. Preparation for GO-Au nanosheet

GO powder was purchased from Cheap Tube Inc., synthesized by a modified Hummer's method. Chemical analysis of GO used here can be found in previous report [28]. 1 mg of the GO powder (20% functionalized [28]) was mixed with 20 mL of deionized water, which was then slowly stirred for 4 weeks using a magnetic stirrer at 350 rpm (Cole-Parmer Stable Temp). The upper portion of the solution was diluted and centrifuged at 3000 rpm for 10 min (Eppendorf MiniSpin) after stirring. The aqueous solution after the previous centrifugal process was further centrifuged at 5000 rpm for 10 min (Eppendorf Mini Spin). Precipitates of GO from the previous solution was then diluted with deionized water. Citrate stabilized 5 nm AuNPs (purchased from Sigma Aldrich) was filtered (Fisher brand Q2 Filter Paper) and a 5 min sonication (Branson M1800 syndicator) was followed to remove large citrate molecules and avoid agglomerations of particles in the gold solution. To achieve a uniform distribution of AuNPs on GO sheets, citrate-stabilized AuNP (85 μl, 6.94 wt%) was added to GO (100 μl, 11.5 wt% exfoliated and diluted GO) and stabilized for 30 min to allow GO to attract AuNPs. The GO nanosheets prepared in this method were polycrystalline multilayers with a lateral size on the order of tens of microns as reported in our previous work [31]. The suspended nanosheet is a multilayer single flake covering the gap between the actuation shuttles. Previous loading-unloading of the GO nanosheets proved no obvious slippage among layers or from the substrate [28]. The thickness of the GO nanosheet was measured to be ~79 nm by electron energy loss spectroscopy (Supplementary Information Fig. S1).

4.2. Scanning transmission electron microscopy

In situ tensile testing was performed in a Hitachi HF-3300 scanning/transmission electron microscope operated at 300 keV in scanning mode (STEM) with simultaneous observation of SE and HAADF images. The probe current was 38 pA and the convergence angle was 10 mrad. The collection angle of the HAADF detector was 80–430 mrad. The images were captured in the dimension of 1200 × 1200 pixels with pixel size of 0.3 nm × 0.3 nm. A control experiment was performed to make sure the measured strain was not induced by electron beam (Fig. S2).

4.3. Error analysis

To evaluate the accuracy of the image processing algorithm for extracting centroids, we applied the same algorithm to extract the centroid of the scale bar in the same image as the gold particles. To provide the ground truth, manual measurement was performed on a zoomed image with the best care. Taking the edge of the scale bar as the origin, manual benchmark gave the centroid position of 167.5 pixels, while the algorithm gave the centroid position as 167 pixels, yielding the measurement error of 0.5 pixel/167.5 pixels = 0.30%. The measurement errors in centroid positions propagate through strain calculation. According to Eq. (2), the local strain is calculated in the form of $strain = F(y_1, y_2, y_3, y_4) = \frac{(y_1-y_2)-(y_3-y_4)}{(y_3-y_4)}$ and each y has an error of 0.30% independently. The propagated error in strain mapping follows: $\delta F = \sqrt{\sum_{i=1}^{4}\left(\frac{\partial F}{\partial y_i}\delta y\right)^2} = \frac{\sqrt{2}\delta y\sqrt{(y_1-y_2)^2+(y_3-y_4)^2}}{(y_3-y_4)^2}$, where δy is the absolute error and $\frac{\delta y}{(y_3-y_4)} = 0.30\%$ from previous analysis. Assuming a strain of 5%, which is the maximum strain in Fig. 3, the error in strain mapping is 0.62%. Additionally, as GO and AuNPs are not chemically bonded, there might be slight relative movements of AuNPs with respect to GO during the tensile test, which might introduce errors to the strain maps. However, based on the experimental observation and the strain mapping results, the relative motion was minimal and thus, the binding was strong. Furthermore, as the suspended nanosheet might not be perfectly taut before strain was applied, part of the strain energy might be used for flattening the nanosheet, which can introduce error to the strain maps. However, such pre-strain should be minimal because the entire nanosheet was very flat as evidenced by that fact that it was on the same focal plane even when imaged at high magnification in TEM.

Acknowledgements

The authors acknowledge financial support from the Natural Sciences and Engineering Research Council of Canada (NSERC) through Discovery Grants (Y.S, and T.F.) and a Collaborative Research and Development grant (Y.S.); from Ontario Research Funds – Research Excellence (Y.S.), the Ontario Ministry of Research and Innovation Early Researcher Award (T.F.), the Erwin Edward Hart Professorship to T.F., the Canada Foundation for Innovation (T.F.) and the Canada Research Chairs Program (Y.S.). TEM analysis was conducted at Ontario Center for the Characterization of Advanced Materials (OCCAM). The authors thank Tongqi Zhu (undergraduate student in Engineering Science Program, University of Toronto), Jane Y. Howe (University of Toronto and Hitachi High Tech) and Sal Boccia (OCCAM) for technical assistance and discussions.

Appendix A. Supplementary data

Supplementary data associated with this article can be found, in the online version, at doi:10.1016/j.apmt.2018.11.010.

References

[1] J. Li, Z. Shan, E. Ma, Elastic strain engineering for unprecedented materials properties, MRS Bull. 39 (2) (2014) 108–114.
[2] B. Pan, K. Qian, H. Xie, A. Asundi, Two-dimensional digital image correlation for in-plane displacement and strain measurement: a review, Meas. Sci. Technol. 20 (6) (2009) 062001.
[3] D.J. White, W.A. Take, M.D. Bolton, Soil deformation measurement using particle image velocimetry (PIV) and photogrammetry, Geotechnique 53 (7) (2003) 619–631.
[4] S. Lee, J. Hwang, M.R. Shankar, S. Chandrasekar, W.D. Compton, Large strain deformation field in machining, Metall. Mater. Trans. A 37 (5) (2006) 1633–1643.
[5] L. Chevalier, S. Calloch, F. Hild, Y. Marco, Digital image correlation used to analyze the multiaxial behavior of rubber-like materials, Eur. J. Mech. 20 (2) (2001) 169–187.
[6] H.I. Rasool, C. Ophus, W.S. Klug, A. Zettl, J.K. Gimzewski, Measurement of the intrinsic strength of crystalline and polycrystalline graphene, Nat. Commun. 4 (2013) 2811.
[7] V.B. Ozdol, C. Gammer, X.G. Jin, P. Ercius, C. Ophus, J. Ciston, A.M. Minor, Strain mapping at nanometer resolution using advanced nano-beam electron diffraction, Appl. Phys. Lett. 106 (25) (2015) 253107.
[8] M. Yagmurcukardes, C. Bacaksiz, E. Unsal, B. Akbali, R.T. Senger, H. Sahin, Strain mapping in single-layer two-dimensional crystals via Raman activity, Phys. Rev. B 97 (11) (2018) 115427.
[9] Y. Han, K. Nguyen, M. Cao, P. Cueva, S. Xie, M.W. Tate, P. Purohit, S.M. Gruner, J. Park, D.A. Muller, Strain mapping of two-dimensional heterostructures with subpicometer precision, Nano Lett. 18 (6) (2018) 3746–3751.

[10] P.B. Hirsch, M.J. Whelan, A kinematical theory of diffraction contrast of electron transmission microscope images of dislocations and other defects, Philos. Trans. R. Soc. Lond. A 252 (1017) (1960) 499–529.
[11] P.J. Phillips, M.C. Brandes, M.J. Mills, M. De Graef, Diffraction contrast STEM of dislocations: imaging and simulations, Ultramicroscopy 111 (9–10) (2011) 1483–1487.
[12] K. Müller, A. Rosenauer, M. Schowalter, J. Zweck, R. Fritz, K. Volz, Strain measurement in semiconductor heterostructures by scanning transmission electron microscopy, Microsc. Microanal. 18 (5) (2012) 995–1009.
[13] J.M. Zuo, J.C.H. Spence, Strain Measurements and Mapping, Advanced Transmission Electron Microscopy, Springer, 2017, pp. 553–580.
[14] K. Elibol, B.C. Bayer, S. Hummel, J. Kotakoski, G. Argentero, J.C. Meyer, Visualising the strain distribution in suspended two-dimensional materials under local deformation, Sci. Rep. 6 (2016) 28485.
[15] G. Wang, Z. Dai, Y. Wang, P. Tan, L. Liu, Z. Xu, Y. Wei, R. Huang, Z. Zhang, Measuring interlayer shear stress in bilayer graphene, Phys. Rev. Lett. 119 (3) (2017) 036101.
[16] F. Bei, X. Hou, S.L.Y. Chang, G.P. Simon, D. Li, Interfacing colloidal graphene oxide sheets with gold nanoparticles, Chemistry 17 (21) (2011) 5958–5960.
[17] J.Y. Howe, D. Yin, T. Filleter, Y. Sun, A MEMS device for fracture toughness measurement of 2D nano films under TEM imaging, in: 2017 19th International Conference on Solid-State Sensors, Actuators and Microsystems (TRANSDUCERS), IEEE, 2017, pp. 750–753.
[18] C. Cao, J.Y. Howe, D. Perovic, T. Filleter, Y. Sun, In situ TEM tensile testing of carbon-linked graphene oxide nanosheets using a MEMS device, Nanotechnology 27 (28) (2016) 28lt01.
[19] M. Sezgin, B. Sankur, Survey over image thresholding techniques and quantitative performance evaluation, J. Electron. Imaging 13 (1) (2004) 146–166.
[20] K. Erickson, R. Erni, Z. Lee, N. Alem, W. Gannett, A. Zettl, Determination of the local chemical structure of graphene oxide and reduced graphene oxide, Adv. Mater. 22 (40) (2010) 4467–4470.
[21] C. Cao, M. Daly, C.V. Singh, Y. Sun, T. Filleter, High strength measurement of monolayer graphene oxide, Carbon 81 (2015) 497–504.
[22] D.A. Dikin, S. Stankovich, E.J. Zimney, R.D. Piner, G.H.B. Dommett, G. Evmenenko, S.T. Nguyen, R.S. Ruoff, Preparation and characterization of graphene oxide paper, Nature 448 (7152) (2007) 457–460.
[23] C. Cao, S. Mukherjee, J.Y. Howe, D.D. Perovic, Y. Sun, C.V. Singh, T. Filleter, Nonlinear fracture toughness measurement and crack propagation resistance of functionalized graphene multilayers, Sci. Adv. 4 (4) (2018) eaao7202.
[24] T. Lee, F.A. Mas'ud, M.J. Kim, H. Rho, Spatially resolved Raman spectroscopy of defects, strains, and strain fluctuations in domain structures of monolayer grapheme, Sci. Rep. 7 (1) (2017) 16681.
[25] X. Zou, B.I. Yakobson, An open canvas—2D materials with defects, disorder, and functionality, Acc. Chem. Res. 48 (1) (2015) 73–80.
[26] X. Wei, L. Mao, R.A. Soler-Crespo, J.T. Paci, J. Huang, S.T. Nguyen, H.D. Espinosa, Plasticity and ductility in graphene oxide through a mechanochemically induced damage tolerance mechanism, Nat. Commun. 6 (2015) 8029.
[27] G.-H. Lee, R.C. Cooper, S.J. An, S. Lee, A. van der Zande, N. Petrone, A.G. Hammerberg, C. Lee, B. Crawford, W. Oliver, J.W. Kysar, J. Hone, High-strength chemical-vapor-deposited graphene and grain boundaries, Science 340 (6136) (2013) 1073–1076.
[28] C. Cao, M. Daly, B. Chen, J.Y. Howe, C.V. Singh, T. Filleter, Y. Sun, Strengthening in graphene oxide nanosheets: bridging the gap between interplanar and intraplanar fracture, Nano Lett. 15 (10) (2015) 6528–6530.
[29] P. Zhang, L. Ma, F. Fan, Z. Zeng, C. Peng, P.E. Loya, Z. Liu, Y. Gong, J. Zhang, X. Zhang, P.M. Ajayan, T. Zhu, J. Lou, Fracture toughness of graphene, Nat. Commun. 5 (2014) 3782.
[30] Y. Yang, X. Li, M. Wen, E. Hacopian, W. Chen, Y. Gong, J. Zhang, B. Li, W. Zhou, P.M. Ajayan, Q. Chen, T. Zhu, J. Lou, Brittle fracture of 2D $MoSe_2$, Adv. Mater. 29 (2) (2017) 1604201.
[31] M. Daly, C. Cao, H. Sun, Y. Sun, T. Filleter, C.V. Singh, Interfacial shear strength of multilayer graphene oxide films, ACS Nano 10 (2) (2016) 1939–1947.